




# Scaling relations for globular cluster systems in early-type galaxies – III. The inner flattening of the radial distributions

Juan Pablo Caso<sup>1,2</sup> , Ana Inés Ennis<sup>3,4</sup>  and Bruno Javier De Bórtoli<sup>1,2</sup> 

<sup>1</sup>*Facultad de Ciencias Astronómicas y Geofísicas de la Universidad Nacional de La Plata, and Instituto de Astrofísica de La Plata (CCT La Plata – CONICET, UNLP), Paseo del Bosque S/N, B1900FWA La Plata, Argentina*

<sup>2</sup>*Consejo Nacional de Investigaciones Científicas y Técnicas, Godoy Cruz 2290, C1425FQB Ciudad Autónoma de Buenos Aires, Argentina*

<sup>3</sup>*Waterloo Centre for Astrophysics, University of Waterloo, 200 University Avenue West, Waterloo, Ontario N2L 3G1, Canada*

<sup>4</sup>*Perimeter Institute for Theoretical Physics, Waterloo, Ontario N2L 2Y5, Canada*

Accepted 2023 November 16. Received 2023 November 16; in original form 2023 October 20

## ABSTRACT

The current properties of globular cluster systems (GCSs) in the nearby Universe are a consequence of an evolutionary history ruled by accretion and disruption processes. The analysis of scaling relations for GCSs is crucial for understanding the relevance of different physical processes involved in their origin and subsequent survival. In this work, radial profiles are calculated for a sample of GCSs associated with nearby massive galaxies. This is supplemented with results from our previous papers, achieving a total sample of 53 GCSs with radial profiles homogeneously calculated, and spanning more than two orders of magnitude in stellar mass of the host galaxy. Scaling relations involving different parameters of the GCSs are obtained for the entire sample, and their significance in terms of different scenarios is considered. Finally, the results are analysed in the literature context.

**Key words:** galaxies: elliptical and lenticular, cD – galaxies: evolution – galaxies: haloes – galaxies: star clusters: general.

## 1 INTRODUCTION

Globular clusters (GCs) are compact stellar systems that occupy the massive end of the stellar cluster mass function. Most of them are between 8 and 10 Gyr old (e.g. Usher et al. 2019; Fahrion et al. 2020), meaning that they formed around the epoch at which the cosmic star formation rate density peaked (Madau & Dickinson 2014). They are present in galaxies of different morphologies, and span a wide range of masses (Harris, Harris & Hudson 2015; Lim et al. 2018), suggesting that they are valuable tracers of the evolution of galaxies. Moreover, the properties of globular cluster systems (GCSs) have been shown to be closely linked to those of their host galaxy, in particular through a variety of scaling relations.

A significant one is the linear relation between the mass enclosed in a GCS and the halo mass of the host galaxy (Hudson, Harris & Harris 2014; Forbes et al. 2018). This persists over several orders of magnitude in halo mass, and it is still present when GC subpopulations are considered separately (Harris, Harris & Hudson 2015). It has been described as a natural consequence of the hierarchical assembly of haloes (El-Badry et al. 2019), which is supported by the presence of second-order environmental effects in several scaling relations for central and satellite galaxies in clusters (De Bórtoli et al. 2022, hereafter *Paper II*). A striking example is NGC 7507, a field elliptical whose kinematics imply that it is deficient in dark matter (Salinas et al. 2012; Lane, Salinas & Richtler 2015), and whose GCS is rather poor in comparison with ellipticals of similar stellar mass (Caso et al. 2013). A possible interpretation for this is that the evolution

of GCSs is ruled by the mass of the dark matter halo, decoupled from the stellar component of the galaxy. In this way, the observed scaling relations between the properties of GCSs and the stellar mass of the host galaxies (e.g. Harris, Harris & Alessi 2013; Caso et al. 2019, hereafter *Paper I*) come from the non-linear behaviour of the stellar-to-halo mass relation across cosmic times (e.g. Légrand et al. 2019; Girelli et al. 2020). Beyond its population, several properties of GCSs suggest a tight connection between its evolution and the main body of the galaxy, for instance (i) the increase in the relevance of the red subpopulation in more massive galaxies (e.g. Peng et al. 2006; Cho et al. 2012), (ii) the correlation of the stellar mass of the galaxy with the dispersion and turnover luminosity of the globular cluster luminosity function (GCLF; Villegas et al. 2010; Harris et al. 2014b), and (iii) GC subpopulations differing in behaviour at large scales of their photometrical and kinematical distributions in bright ellipticals (e.g. Schuberth et al. 2010; Caso, Bassino & Gómez 2017), possibly showing that they are associated with distinct components of the galaxy. Hence, a combination of the mass accretion history and intrinsic evolutionary processes is very likely responsible for the current properties in the GCS hosted by nearby galaxies.

The improvement of computational capabilities has facilitated the use of simulations to study the formation and subsequent evolution of GCs in a cosmological context (e.g. Kravtsov & Gnedin 2005; Bekki & Yahagi 2006; Kruijssen 2014, and subsequent studies). However, it is still unclear whether the birth of old GCs was driven by galaxy mergers, accretion of cold gas through filaments, or just regular star formation (Kim et al. 2018; Mandelker et al. 2018). A mix of these pathways rather than a single one of them is suggested by nearby merger remnants (Strader, Brodie & Forbes 2004; Richtler et al. 2017; Sesto et al. 2018) as well as recent

\* E-mail: [jpcaso@fcaglp.unlp.edu.ar](mailto:jpcaso@fcaglp.unlp.edu.ar)

high-redshift observations of proto-GCs (e.g. Vanzella et al. 2022). It is currently understood that GCs formed within high-pressure clouds that experienced compression by feedback-driven winds or collisions with other clouds (Ma et al. 2020). Both observations and simulations of groups of nearby star clusters suggest that the hierarchical assembly played a role in the formation of the proto-GCs (e.g. Tornamenti et al. 2022; Della Croce et al. 2023), but numerous questions remain unanswered, including the initial stellar mass function that governed their formation (e.g. Fukushima & Yajima 2023, and references therein).

These efforts to determine the conditions and mechanisms responsible for the GC formation are typically constrained by the observed properties of nearby GCSs, but a key consideration to be made is that the observed GCSs are made up of the objects that survived the evolution of their host galaxy (e.g. Mieske, Küpper & Brockamp 2014; Rossi, Bekki & Hurley 2016; Choksi & Gnedin 2019). The extreme environmental conditions that lead to the origin of GCs might also favour their disruption during the first Gyr after cluster formation (e.g. Li & Gnedin 2019). In this scenario, mergers facilitate the survival of some GCs by redistributing them to the halo, thus linking the build-up of GCSs to the merging history of their host galaxy (e.g. Choksi & Gnedin 2019; Kruijssen et al. 2019). Our understanding of the long-term disruption of GCs is limited, and its consequences in the current properties of GCSs are hardly established, with numerical studies arriving at opposite conclusions (e.g. El-Badry et al. 2019; Bastian et al. 2020). In particular, Capuzzo-Dolcetta & Mastrobuono-Battisti (2009) attributed the observed flattening in the inner regions of the GC radial profile to long-term dynamical friction and estimated the number of eroded GCs from the comparison with the stellar population profile of the galaxy. More recently, a few numerical studies have addressed this topic (e.g. Brockamp et al. 2014; Reina-Campos et al. 2022) as a product of simulations that differ in the significance assigned to various disruption mechanisms.

Another clear example of the impact of disruption in scaling relations at  $z = 0$  is the initial mass function for GCs, which in numerical simulations is modelled as a power law with exponent  $-2$  (e.g. Kruijssen 2015; Rossi, Bekki & Hurley 2016) or a Schechter function (e.g. Choksi & Gnedin 2019), based on observational results of star cluster formation at redshift  $z = 0$  (e.g. Lieberz & Kroupa 2017, and references therein). This differs significantly from the GCLF measured in the Local Universe (e.g. Villegas et al. 2010; Harris et al. 2014b). A considerable effort has been made in the past decade to constrain the formation theories of GCs (see the review from Beasley 2020). In this sense, literature results suggest correlations between the galactocentric distance ( $r_{\text{gal}}$ ) and both the average half-light radius of GCs (Jordán et al. 2005) and the turnover luminosity in GCLF (Harris et al. 2014b) in massive ellipticals. Both gradients can be interpreted as evidence of the relevance of tidal interactions in the disruption of GCs, but more evidence is needed to constrain these models. Although the inner regions of massive galaxies constitute an ideal test bench for GC disruption, there are only a few studies addressing this issue from both observational and numerical sides (e.g. Capuzzo-Dolcetta & Mastrobuono-Battisti 2009; Brockamp et al. 2014).

It is clear that the different disruption mechanisms experienced by GCs during their lifetime strongly influence the current properties of the GCSs. These processes surpass the early destruction of GCs during their first Gyr of existence, and accurate modelling would enhance our understanding of formation theories and their cosmological interpretation. Analysing the properties of nearby GCSs is essential to achieve this.

In this study, we present the analysis of the inner GCS radial profile for a sample of nearby ellipticals that present several thousands of GCs, complementing our previous studies. In Paper I, several scaling relations for GC radial profiles were revisited and extended towards lower stellar masses, based on the homogeneous analysis of the GCSs in a sample of nearby early-type galaxies (ETGs) with intermediate luminosity, and supplemented with results from the literature. The sample was enlarged in Paper II, which focused on the relevance of the environment in the evolution of GCS and how it impacts the scaling relations. This work extends the sample analysed in a homogeneous manner to the massive end of the stellar mass function, and focuses on the properties of the GCS at galactocentric distances comparable to the effective radius of the galaxy, in order to shed some light on our understanding of disruption mechanisms.

The paper is organized as follows: Section 2 describes the observations and data reduction, in Sections 3 we present the results, and Section 4 is devoted to the discussion of the GCS scaling relations in the literature context. Finally, in Section 5 our conclusions are summarized.

## 2 OBSERVATIONAL DATA AND REDUCTION

The GCSs in the sample analysed in this paper are hosted by bright ETGs from the nearby clusters in Virgo ( $D \approx 17$  Mpc; Mei et al. 2007) and Fornax ( $D \approx 20$  Mpc; Blakeslee et al. 2009), as well as two intermediate-luminosity galaxies from the Fornax cluster, NGC 1374 and NGC 1427, which were not included in our previous studies. A list of properties of the galaxies is presented in Table 2, including magnitudes in several bands and distances. The data set consists of photometric observations carried out with the Advanced Camera for Surveys (ACS) in the Wide Field Channel, mounted at the *Hubble Space Telescope* (HST) and publicly available at the Mikulski Archive for Space Telescopes,<sup>1</sup> originally observed as part of programmes 9401 (Côté et al. 2004) and 10217 (Jordán et al. 2007). The observations correspond to filters *F475* and *F850*, widely used to study GCSs in the literature, and the total exposure times are 750 and 1120 s, respectively.

These observations are deep enough to obtain accurate photometry for the GCSs up to more than 1 mag below the turnover magnitude (TOM) of the globular cluster luminosity function (GCLF), including typically more than 80 per cent of the GC population for each galaxy (see Villegas et al. 2010, for more details on the GCLF of the galaxies in Virgo and Fornax clusters). The fields are centred on the galaxies, with a field-of-view (FOV) of  $202 \times 202$  arcsec<sup>2</sup> and a pixel scale of 0.05 arcsec.

### 2.1 Photometry and selection of GC candidates

First, the stellar component of the galaxies is fitted in both filters, using the task ELLIPSE within IRAF, and a synthetic model is generated and subtracted from the original image to facilitate the detection of GC candidates. Following Paper I, a first catalogue of sources is made in each filter by means of SExtractor (Bertin & Arnouts 1996), assuming as a source every detection of at least three connected pixels above a threshold of  $3\sigma$ . Aperture photometry, with

<sup>1</sup>Based on observations made with the NASA/ESA *Hubble Space Telescope*, obtained from the data archive at the Space Telescope Science Institute. STScI is operated by the Association of Universities for Research in Astronomy, Inc. under NASA contract NAS 5-26555.

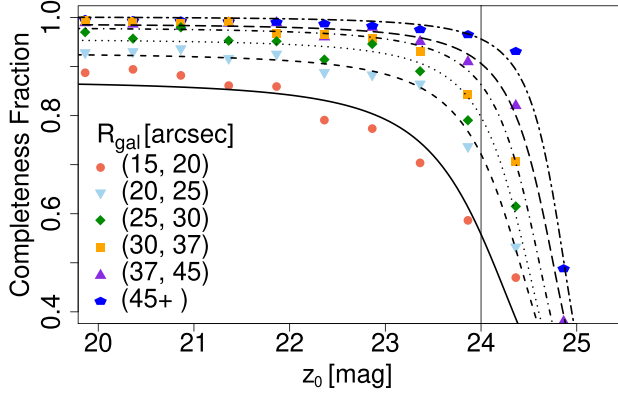


**Figure 1.** Completeness as a function of  $z_0$  magnitude for M87, obtained from 120 000 artificial stars. The completeness curves are calculated in six galactocentric ranges, and the fits correspond to equation (1). The vertical line at  $z_0 = 24$  mag indicates the magnitude limit assumed for the analysis. An analogue analysis is performed for the other galaxies in the sample.

an aperture radius of 5 px, is also performed in this step. Sources with elongation larger than 2 and presenting full width at half-maximum larger than 5 px are rejected, considering that GC-like objects at the distances to Virgo and Fornax galaxies are expected to be marginally resolved in *HST/ACS*, and present low eccentricities (see Paper I, and references therein). Similar criteria have been previously applied to select GC candidates in these observations (e.g. Jordán et al. 2004, 2007).

The structural parameters of the objects with a signal-to-noise ratio larger than 50 are derived using ISHAPE (Larsen 1999), assuming a King profile (King 1962, 1966) with a concentration parameter of  $c = 30$ . Then, the results are used to split the sample into ranges of effective radius ( $r_{\text{eff}}$ ), from 1.5 to 4.5 pc, which comprises 80–90 per cent of the GC population, according to the distributions derived by Jordán et al. (2005) and Masters et al. (2010) for Virgo and Fornax galaxies, respectively. Aperture corrections are calculated for each group of objects in order to quantify their change with  $r_{\text{eff}}$  that scarcely represents 0.05 mag for the entire range. Since this change is not significant for our goals, we adopt mean aperture corrections, estimated from bright objects with  $r_{\text{eff}} = 3 \pm 0.25$  pc. This procedure was also applied in Papers I and II.

The instrumental magnitudes ( $F475$ ,  $F850$ ) are calibrated to ( $g$ ,  $z$ ) bands based on the zero-points magnitudes published by Sirianni et al. (2005),  $ZP_{F475} = 26.068$  and  $ZP_{F850} = 24.862$ . Then, the Schlafly & Finkbeiner (2011) calibration is adopted to correct by Galactic extinction. Finally, we select as GC candidates those sources with colours in the range  $0.6 \text{ mag} < (g - z)_0 < 1.7 \text{ mag}$ , in agreement with previous studies in these bands (e.g. Jordán et al. 2005; Cho et al. 2012), and  $z_0 < 24$  mag, to avoid the drop in completeness (see next section).

## 2.2 Completeness analysis

The photometric completeness for each galaxy is obtained from the addition of artificial stars to the images in both bands. A total of 120 000 stars are added along 1800 runs, spanning the colour range of GCs and  $20 < z_0 < 25$  in brightness. The photometry is performed in the same manner as for the science fields, and the catalogue of measured artificial stars is used to derive the completeness curves in six different galactocentric ranges (Fig. 1). The fainter magnitude

**Table 1.** Parameters of the analytical function described in equation (1), fitted to the completeness curves derived for different galactocentric regimes in the case of M87. Analogue analyses were performed on the rest of the galaxies listed in Table 2.

Radial regime (arcsec)	$\alpha$	$\beta$	$m_0$ (mag)
15–20	1.12	0.44	24.25
20–25	1.45	0.46	24.45
25–30	1.76	0.48	24.50
30–37	1.90	0.49	24.60
37–45	2.00	0.49	24.75
45+	2.50	0.50	24.85

limit is selected at  $z_0 = 24$  mag, at which completeness levels typically fall below 90 per cent for distances to the galaxy centre larger than 30 arcsec, and around 70 per cent for lower distances. An analytical function is fitted to the completeness curve, similar to that used by Harris et al. (2009):

$$f(m) = \beta \left( 1 - \frac{\alpha(m - m_0)}{\sqrt{1 + \alpha^2(m - m_0)^2}} \right) \quad (1)$$

with  $\beta$ ,  $\alpha$ , and  $m_0$  free parameters. The galaxies present slightly different parameters, depending on their surface brightness profile, but the overall behaviour is similar, with completeness approaching 1 for artificial stars brighter than  $z_0 = 23$  mag and galactocentric radii larger than 30 arcsec, but falling for inner radii. For comparison purposes, Table 1 shows the parameters fitted to the completeness curves of M87.

## 3 RESULTS

### 3.1 Radial profiles of globular cluster systems

There are several functional expressions used in the literature to fit the radial profile of a GCS. Following Papers I and II, the modified Hubble profile (e.g. Binney & Tremaine 1987; Bassino & Caso 2017) is chosen in this study,

$$n(r) = a \left( 1 + \left( \frac{r}{r_0} \right)^2 \right)^{-b}, \quad (2)$$

which behaves as a power law with an exponent  $2b$  at large galactocentric distances, but flattens below the core radius  $r_0$ , representing the depletion of GCs usually found in bright ellipticals.

The projected GC density distributions are obtained from concentric circular annuli, and corrected by differential completeness through the analysis described in Section 2.2. The results for each galaxy are shown in Fig. 2 with black squares. The contamination is derived from ACS fields from the respective clusters, centred on dwarf galaxies with poor GCSs, according to literature results (Peng et al. 2008; Liu et al. 2019). We concluded that this correction is negligible for the majority of the galaxies in this sample, considering the large population of the GCSs and the central region analysed in this work. The radial binning is constant on a logarithmic scale for all the profiles, with a typical value of  $\Delta \log_{10} r = 0.1$ , with  $r$  in arcmin.

The extension of the GCSs in massive galaxies usually exceeds 100 kpc (e.g. Bassino et al. 2006b; Peng et al. 2011; Caso, Bassino & Gómez 2017), and the limited FOV of *HST/ACS* scarcely represents a tenth of it for our nearby galaxies. Hence, to obtain accurate radial profiles, only the central density  $a$  and the core radius  $r_0$  from the

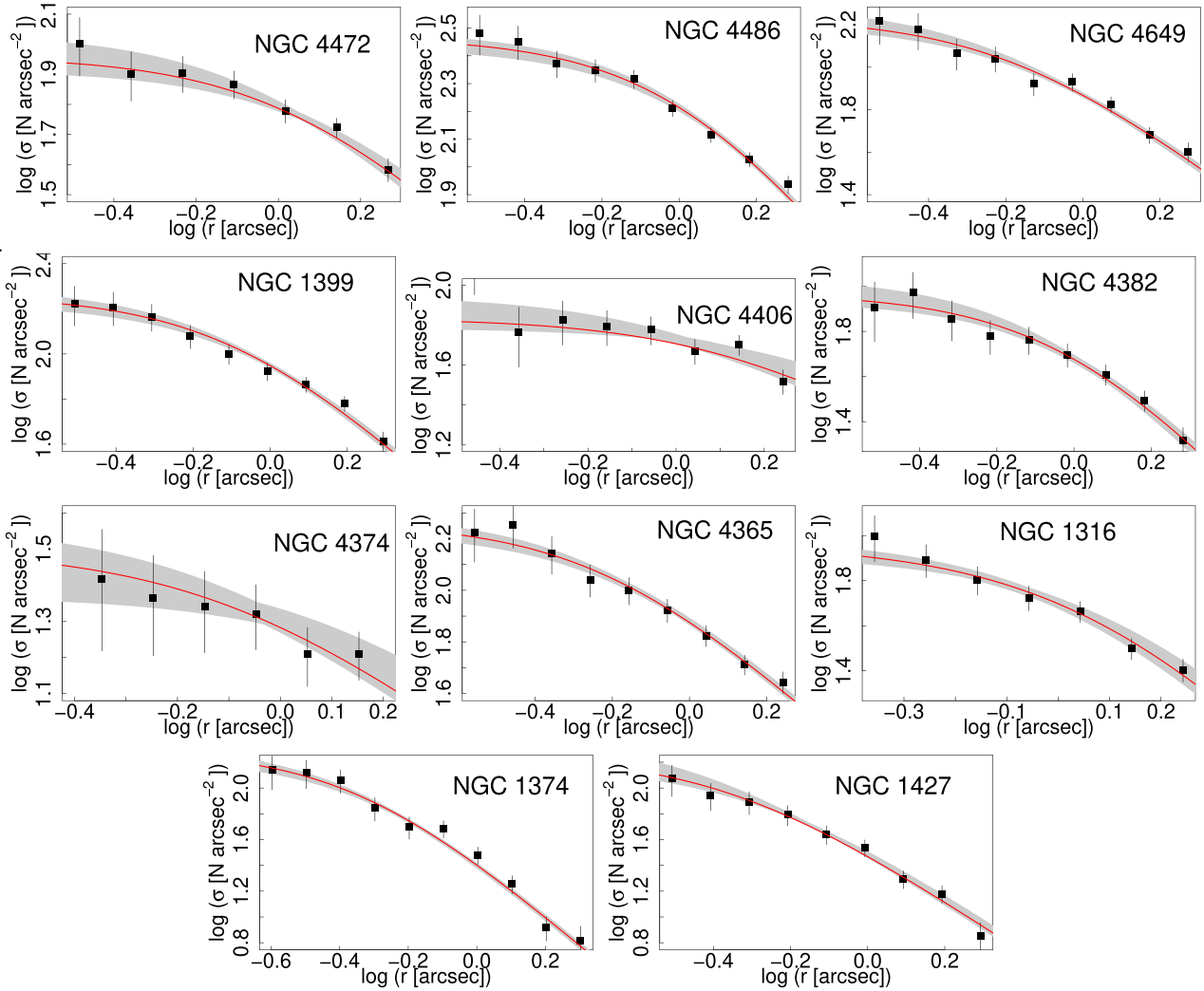


**Figure 2.** Projected radial distribution for the GCS analysed in this study. The red solid lines represent the fitted modified Hubble profile, with fixed slope (obtained from the literature). The grey regions show the variations from several fits performed by shifting the bin breaks (see text for further details).

Hubble profile are fitted to the radial distributions. The slope  $b$  is fixed to values derived by large-scale studies from the literature. This does not introduce uncertainties in our analysis because the slope of the radial profiles is usually accurately fitted in these studies and their major issues come with the decrease of completeness towards the centre of the galaxy. Small shifts are applied ten times to the bin breaks and the parameters of the Hubble profile are fitted in each step to account for noise uncertainties. The changes in the Hubble modified profile are represented by the shaded regions in Fig. 2. The definitive parameters, listed in Table 2, are obtained through the weighed mean of those fitted in each individual run, and correspond to the solid curve in Fig. 2. The assumed  $b$  slopes and their references are also listed in the table.

In the case of the most populated systems, the radial profile is also fitted for different ranges of GC magnitudes. The GC sample is divided into quartiles through the integration of the Gaussians fitted by Villegas et al. (2010) to their GCLF. The photometry depth allows us to derive radial profiles for the three brightest quartiles, which are represented in Fig. 3, and their core radius,  $r_0$ , are listed in Table 3. In the four cases, the core radius increases towards fainter magnitudes,

representing approximately the effective radius of the host galaxy ( $r_{\text{eff,gal}}$ ) for the second quartile.

### 3.2 Scaling relations for GCSs

In this section, the properties of the inner region of GCSs are derived as a function of several parameters of the host galaxies. The sample of ETGs analysed in this paper is complemented with those profiles presented in our previous studies: 17 GCSs from Paper I and 18 from Paper II, associated with ETGs in the clusters of Virgo and Fornax, plus 7 GCS from Paper I, corresponding to ETGs located in low-density environments. This results in 53 ETGs with photometry in filters  $g$  and  $z$  derived in the same manner, from images presenting similar depth. This latter point is important, considering that the efficiency of the physical processes involved in the GC disruption is assumed to vary with the mass of the GCs.

The evolution of the GCSs is tightly related to that of the stellar population of their host galaxies; hence, the comparison with their stellar mass ( $M_*$ ) is straightforward. As well as in our previous papers,  $M_*$  is assumed as the mean of the masses derived from the luminosity in  $J$  and  $K$  bands, using the mass-to-light ratios ( $M/L$ ) from Bell

**Table 2.** Galaxies under analysis on this paper, listed in decreasing  $B$ -band luminosity. The apparent magnitudes in several filters (columns 2–5) are obtained from NASA/IPAC Extragalactic Database (NED) and the reddening corrections correspond to the recalibration by Schlafly & Finkbeiner (2011). The distances correspond to SBF measurements listed in NED, typically from Tully et al. (2013) or Blakeslee et al. (2009). Columns 8–11 correspond to the parameters from the modified Hubble profiles, where  $a$  and  $r_0$  are fitted to the GCS radial profiles, and the slope ( $b$ ) is assumed from large-scale studies available in the literature. Column 10 corresponds to the core radius expressed in kiloparsecs, assuming the distances indicated in column 7. Its uncertainty comes from that of the parameter fitted to the data, and the typical error in the distances, assumed as 5 per cent. The effective radius of the galaxy ( $r_{\text{eff,gal}}$ ) and its total GC population ( $N_{\text{GCS}}$ ) also comes from the literature. The central velocity dispersion ( $\sigma_0$ ) is taken from the HyperLeda data base.

Name	$B$ (mag)	$V$ (mag)	$J$ (mag)	$K$ (mag)	$E_{(B-V)}$ (mag)	$D$ (Mpc)	$a$	$r_0$ (arcmin)	$r_0$ (kpc)	$b$	$r_{\text{eff,gal}}$ (kpc)	$N_{\text{GCS}}$	$\sigma_0$ (km s $^{-1}$ )
NGC 1316	9.40	8.53	6.45	5.59	0.019	20.8	$2.08 \pm 0.03$	$1.01 \pm 0.06$	$6.1 \pm 0.5$	$1.23^1$	3.5	$2542 \pm 514^2$	223
NGC 4472	9.37	8.41	6.27	5.40	0.020	16.7	$1.92 \pm 0.02$	$1.26 \pm 0.11$	$6.1 \pm 0.6$	$0.64^3$	8.4	$9100 \pm 1000^4$	282
NGC 4486	9.59	8.63	6.72	5.81	0.022	16.7	$2.47 \pm 0.01$	$1.06 \pm 0.03$	$5.1 \pm 0.3$	$0.91^5$	8.4	$14660 \pm 891^6$	323
NGC 4406	9.83	8.90	7.01	6.10	0.026	17.1	$1.84 \pm 0.02$	$1.34 \pm 0.19$	$6.7 \pm 1.0$	$0.62^7$	7.5	$2660 \pm 129^6$	231
NGC 4649	9.81	8.84	6.67	5.74	0.025	16.4	$2.18 \pm 0.01$	$0.79 \pm 0.01$	$3.8 \pm 0.2$	$0.69^8$	5.9	$4690 \pm 980^8$	331
NGC 4382	10.00	9.11	7.06	6.15	0.026	17.9	$1.97 \pm 0.01$	$0.98 \pm 0.04$	$5.1 \pm 0.3$	$0.94^9$	8.9	$1100 \pm 181^6$	176
NGC 4374	10.09	9.11	7.12	6.22	0.036	16.9	$1.51 \pm 0.04$	$0.78 \pm 0.11$	$3.8 \pm 0.2$	$0.55^{10}$	4.5	$4300 \pm 1200^6$	278
NGC 1399	10.60	9.59	7.21	6.31	0.012	20.2	$2.26 \pm 0.01$	$0.83 \pm 0.02$	$4.9 \pm 0.3$	$0.81^{11}$	4.1	$6450 \pm 700^{12}$	332
NGC 4365	11.00	9.60	7.50	6.60	0.021	23.1	$2.26 \pm 0.02$	$0.6 \pm 0.04$	$4.0 \pm 0.3$	$0.67^{13}$	6.4	$6450 \pm 110^{13}$	250
NGC 1427	11.77	10.86	9.03	8.14	0.011	19.6	$2.26 \pm 0.03$	$0.44 \pm 0.02$	$2.5 \pm 0.2$	$1.00^{14}$	3.3	$470 \pm 40^{14}$	155
NGC 1374	12.00	11.08	9.05	8.16	0.012	19.6	$2.29 \pm 0.04$	$0.45 \pm 0.02$	$2.6 \pm 0.2$	$1.15^{15}$	2.5	$360 \pm 17^{15}$	179

*Note.* References: <sup>1</sup>Richtler et al. (2012), <sup>2</sup>Liu et al. (2019), <sup>3</sup>Rhode & Zepf (2001), <sup>4</sup>Durrell et al. (2014), <sup>5</sup>Harris (2009), <sup>6</sup>Peng et al. (2008), <sup>7</sup>Rhode & Zepf (2004), <sup>8</sup>Faifer et al. (2011), <sup>9</sup>fitted on data from Ko et al. (2019), <sup>10</sup>Gómez & Richtler (2004), <sup>11</sup>Bassino et al. (2006b), <sup>12</sup>Dirsch et al. (2003), <sup>13</sup>Blom, Spitler & Forbes (2012), <sup>14</sup>Forte et al. (2001), <sup>15</sup>Bassino, Richtler & Dirsch (2006a).

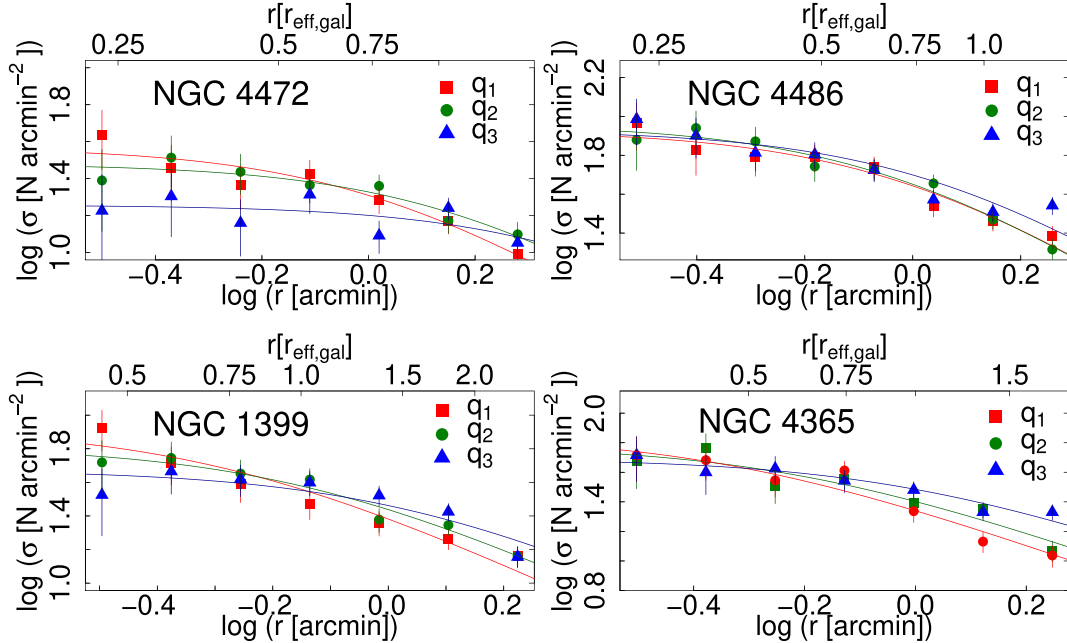


**Figure 3.** Projected radial distribution for the most populated GCSs in the sample, split into quartiles of the GCLF from Villegas et al. (2010). The solid lines represent the fitted modified Hubble profile, with a fixed slope (obtained from the literature). The upper  $x$ -axis is represented in units of the effective radius of the galaxy, following the values indicated in Table 2.

et al. (2003) and the  $(B - V)$  colours, adopting a Salpeter initial mass function (see Table 2, and Papers I and II). The sample spans two orders of magnitude in  $M_*$ , from cluster-dominant galaxies to intermediate-mass ETGs.

The left panel of Fig. 4 shows the core radius ( $r_{0,\text{GCS}}$ ) of the modified Hubble profiles as a function of the  $M_*$  of the galaxy, in logarithmic scale. The different symbols represent those GCSs hosted by galaxies classified as slow rotators (circles, hereafter SRs) and fast rotators (ellipses, hereafter FRs) by Emsellem et al. (2011), Scott et al. (2014), and Iodice et al. (2019). Those galaxies without kinematical information, typically in the Southern Hemisphere, are symbolized with triangles. The colour palette, from light yellow to

dark red, represents increasing values for the colour gradient of the galaxies in the  $(g - z)$  filters for the inner  $r_{\text{eff,gal}}$ ,  $\Delta_{g-z}$ . Following Li et al. (2011), we obtain it through the expression:

$$\Delta_{g-z} = \frac{(g-z)_{r_{\text{eff,gal}}} - (g-z)_{r_0}}{\log r_{\text{eff,gal}} - \log r_0} \quad (3)$$

with  $r_0$  corresponding to 1 arcsec, to avoid central star clusters and differences in cusp/core profiles. The colours are obtained from the Sersic profiles fitted by Ferrarese et al. (2006), and Papers I and II. The majority of the sample has a negative gradient, implying that the galaxy is redder in the centre, but most of them present mild

**Table 3.** Galaxies with populated GCSs, for whom the radial distribution is derived in three magnitude ranges, defined as quartiles of the GCLF. The columns 2–4 present the core radius of the fitted Hubble profile for each quartile, in decreasing order of brightness.

Name	$r_0$ (arcmin)			$r_{\text{eff,gal}}$ (arcmin)
	$q1$	$q2$	$q3$	
NGC 4472	$0.70 \pm 0.11$	$1.10 \pm 0.15$	$2.10 \pm 0.50$	1.2
NGC 4486	$0.92 \pm 0.05$	$0.97 \pm 0.10$	$1.12 \pm 0.15$	1.3
NGC 1399	$0.57 \pm 0.09$	$0.77 \pm 0.08$	$1.40 \pm 0.20$	0.7
NGC 4365	$0.45 \pm 0.1$	$0.69 \pm 0.1$	$0.97 \pm 0.13$	0.9

gradients (i.e.  $|\Delta_{g-z}| < 0.1$ ), which is in agreement with the results from Li et al. (2011) for the early-type galaxies in their sample. If the numerical range spanned by  $\Delta_{g-z}$  is split in halves, the lower one corresponds to galaxies with  $M_*$  from  $8 \times 10^9$  to  $7 \times 10^{10} M_\odot$ , with a mean value of  $\approx 3 \times 10^{10} M_\odot$ , and increasing masses towards less negative gradients, which is in agreement with recent results from Liao & Cooper (2023).

For  $r_{0,\text{GCS}}$  and the  $M_*$ , a Kendall test Kendall (1938) reveals a significant correlation at 99 per cent, and the same result is obtained if only FRs are considered. Following Sereno (2016), a Bayesian linear regression analysis is performed by means of the LIRA package. For the entire sample, it leads to

$$\log_{10}(r_{0,\text{GCS}}) = -3.3 \pm 0.4 + 0.34 \pm 0.04 \times \log_{10}(M_*) \quad (4)$$

represented in Fig. 4 by the solid line, and intrinsic scatter of 0.04 dex.

If only FRs are taken into account, the slope slightly changes to  $0.29 \pm 0.03$ , but an enlarged sample is required to analyse whether there is a different behaviour for SRs and FRs. If the range of  $\Delta_{g-z}$  is divided into halves, the slopes for the intervals of increasing gradients are  $0.21 \pm 0.02$  (dashed line) and  $0.29 \pm 0.04$  (dotted line in Fig. 4), respectively. The slope corresponding to the most negative gradients differs from the general trend. However, it is important to consider that these galaxies correspond to a narrow range in mass.

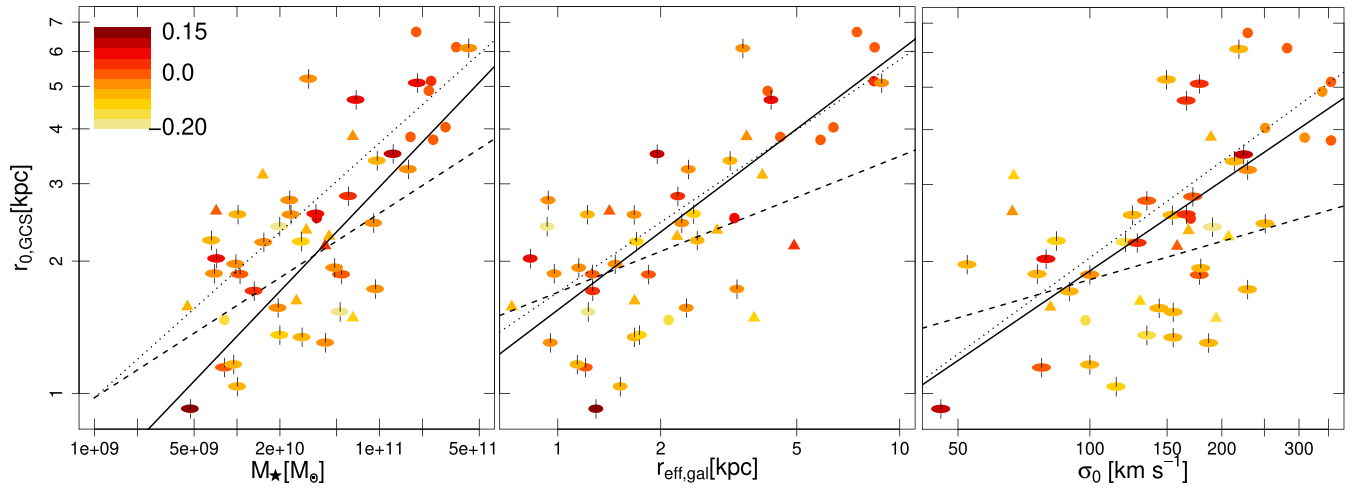


**Figure 4.** *Left panel:* Core radius of the modified Hubble profile of the GCS ( $r_{0,\text{GCS}}$ ), as a function of the stellar mass of the host galaxy ( $M_*$ ). The symbols differentiate between galaxies classified as SRs or FRs (circles and ellipses, respectively), and those lacking of kinematical information (triangles). The colours, from light yellow to dark red, represent increasing values of the colour gradient  $\Delta(g-z)$  for the host galaxy. The solid line results from a Bayesian linear regression fit to the entire sample, while the dashed and dotted lines represent fits for increasing intervals of  $\Delta(g-z)$ . *Middle panel:*  $r_{0,\text{GCS}}$  versus the effective radius of the galaxy ( $r_{\text{eff,gal}}$ ), both in kpc, as listed in Table 2 and A1. The symbol coding is the same as in the left panel, as well as the subgroups represented by each line stroke. *Right panel:*  $r_{0,\text{GCS}}$  versus the central velocity dispersion, obtained from HyperLeda for galaxies analysed in this paper, and from Papers I and II for the rest. The symbol coding is the same as in the previous panels.

Although several studies have focused on the processes that rule the disruption of GCs (e.g. Rossi, Bekki & Hurley 2016; Giersz et al. 2019; Li & Gnedin 2019), only a few of them described the resulting radial profile of the GCS. Brockamp et al. (2014) take into account several mechanisms that may drive the mass-loss of GCs in elliptical galaxies simulated in isolation. The GC radial profiles from their simulations tend to present a central core, due to the efficiency of dissolution processes in the central regions. They found that the mean galactocentric radius at which GCs are destroyed, in units of  $r_{\text{eff,gal}}$ , is inversely proportional to the mass and size of the galaxy. Hence, it is worth it to analyse the connection between these parameters, assuming the  $r_{0,\text{GCS}}$  as a proxy for this radius. The middle panel of Fig. 4 shows the  $r_{0,\text{GCS}}$  as a function of  $r_{\text{eff,gal}}$ , from single Sérsic profiles (see Ferrarese et al. 2006, also Papers I and II). The symbol coding is the same as in the previous plot. A Kendall test reveals a significant correlation at 99 per cent, and the linear regression analysis for the entire sample leads to

$$\log_{10}(r_{0,\text{GCS}}) = 0.19 \pm 0.03 + 0.6 \pm 0.07 \times \log_{10}(r_{\text{eff,gal}}) \quad (5)$$

with an intrinsic scatter of 0.06 dex. This implies that the ratio  $r_{0,\text{GCS}}/r_{\text{eff,gal}}$  is inversely proportional to  $r_{\text{eff,gal}}$ , and through the size-mass relation (e.g. Hon, Graham & Sahu 2023, and references therein) to  $M_*$  of the galaxy. Again, the sample is divided into halves from their colour gradients. For the most negative gradients (dashed line), the fitted slope is  $0.30 \pm 0.2$ , and its large uncertainty reflects the reduced stellar mass spanned by these galaxies. The slope for galaxies with larger  $\Delta(g-z)$  is  $0.53 \pm 0.08$  (dotted lines), in agreement with the general trend.

Some studies focused on GCSs found a correlation between the mass of the central black hole of the host galaxy and the total population of the GCS ( $N_{\text{GCS}}$ ), suggesting a coeval evolution (e.g. Harris, Poole & Harris 2014a; González-Lópezlira et al. 2022). Based on the well-known correlation between stellar velocity dispersions and masses of the central black hole (e.g. van den Bosch 2016; Gaspari et al. 2019), it is worth analysing the evolution of  $r_{0,\text{GCS}}$  versus the central velocity dispersion ( $\sigma_0$ ), which is shown in the

right panel of Fig. 4. For galaxies analysed in this paper,  $\sigma_0$  is listed in Table 2, while the rest of them can be found in Papers I and II. The solid curve corresponds to the linear fit in logarithmic scale for the entire sample,

$$\log_{10}(r_{0,\text{GCS}}) = -1.1 \pm 0.30 + 0.68 \pm 0.13 \times \log_{10}(\sigma_0) \quad (6)$$

but with an intrinsic scatter of 0.11, larger than in the previous cases. The other curves represent the fits when the sample is split into halves of the  $\Delta(g-z)$  range. For the most negative gradients (dashed line), the relation is flatter, with a slope of  $0.30 \pm 0.11$ , becoming steeper for galaxies with larger values of  $\Delta(g-z)$  (dotted lines),  $0.73 \pm 0.13$ , similar to the general trend. The Kendall test implies a significant correlation at 99 per cent, with a  $\tau$  coefficient similar of 0.39, according to that obtained for  $r_{\text{eff,gal}}$ , and lower than the coefficient obtained for  $M_*$ , 0.44. These results suggest that the black hole mass does not lead to a particularly tight correlation with the size of the core of the GCS.

Numerical studies suggested that tidal shocks by close encounters rule the disruption of GCSs in the early stages of their evolution (e.g. Choksi & Gnedin 2019). Although it is assumed that the current conditions in the central regions of early-type galaxies differ from the turbulent environment of discs at high redshift (Kruijssen 2015), the projected stellar density might preserve evidence about the circumstances that enhanced GCSs dissolution in the past. In order to look into this, the surface brightness of the galaxies at  $r_{0,\text{GCS}}$  is obtained from the Sérsic profile fitted to the  $z$  filter ( $\mu_{z,r_0}$ ). However, when analysed across the luminosity range spanned by the galaxies in our sample, we find no correlation with  $r_{0,\text{GCS}}$ . This lack of correlation also prevails if the relations from Bell et al. (2003) are used to convert  $\mu_{z,r_0}$  to projected stellar mass density. The parameter  $\mu_{z,r_0}$  correlates with  $M_*$ , getting brighter towards more massive galaxies, but this emerges from the correlation between  $r_{0,\text{GCS}}$  and  $r_{\text{eff,gal}}$ , and the scaling relation between  $\mu_{\text{eff}}$  and  $M_*$  (or  $M_{V,T}$  in some studies) for early-type galaxies (e.g. Kormendy & Bender 2012; Calderón et al. 2015).

We also analysed the richness in GCSs enclosed by  $r_{0,\text{GCS}}$  as defined by Zepf & Ashman (1993) through the parameter  $T_{N,r_0}$ , calculated as the ratio between the number of GCSs up to  $r_{0,\text{GCS}}$  and the stellar mass enclosed by that radius. The first value is obtained through the integration of the modified Hubble profile, and the stellar mass up to  $r_{0,\text{GCS}}$  emerges from the product of the mean ( $M/L_z$ ) from Bell et al. (2003) and the cumulative projected flux in the  $z$  filter through the integration of the Sérsic profile (Sersic 1968) up to the radius  $r_{0,\text{GCS}}$ , from the expression

$$F(r_p) = 2\pi r_{\text{eff,gal}}^2 b_n^{-2n} I_{\text{eff,gal}} n e^{b_n} \gamma \left[ 2n, b_n \left( \frac{r_p}{r_{\text{eff,gal}}} \right)^{\frac{1}{n}} \right] \quad (7)$$

with  $r_{\text{eff,gal}}$ ,  $I_{\text{eff,gal}}$ , and  $n$ , the parameters of the Sérsic profile.

The upper panel of Fig. 5 shows the fractional richness as a function of the  $M_*$  of the galaxy. The symbol coding is the same as in Fig. 4. This fractional richness deviates from the classical U-shape, with a minimum around  $5 \times 10^{10} M_\odot$ , and the largest values towards both extremes of the mass range. Instead, in this analysis it seems to flatten for the entire mass range, although a correlation cannot be discarded from a Kendall test. After removing the only galaxy with  $T_{N,r_0} > 15$ , the mean results  $5 \pm 3$ . If the sample is restricted to those galaxies that present colour gradients in the upper half of the  $\Delta_{g-z}$  range, the Kendall test rejects a correlation at the 90 per cent of confidence, and the mean results in  $4.2 \pm 1.8$ . The lower panel shows the change in richness between the global parameter, obtained from the population of the GCSs compiled for these galaxies

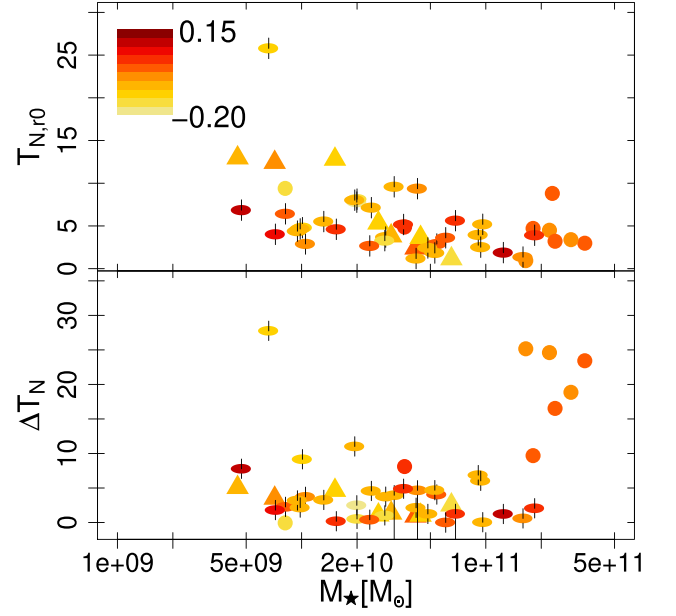


**Figure 5.** Upper panel: Fractional richness for the core of the GCS,  $T_{N,r_0}$  considering the number of GCSs at lower galactocentric distances than  $r_{0,\text{GCS}}$ , and the stellar mass enclosed at that distance. The symbol coding is the same than in the previous figure. Lower panel: Change between the global richness of the GCS, obtained from its total population and the  $M_*$  of the galaxy, and  $T_{N,r_0}$ .

in Papers I and II, and the fractional richness up to  $r_{0,\text{GCS}}$ , represented by  $\Delta T_N$ , as a function of  $M_*$ . The GCSs with the most significant change between  $T_{N,r_0}$  and its total richness are those at the massive end, which is expected from the large contribution of GCSs accreted from satellites to the outer regions of the GCS (e.g. Forbes et al. 2011; Caso, Bassino & Gómez 2017; Ramos-Almendares et al. 2020). For the galaxies fulfilling  $M_* \lesssim 10^{11} M_\odot$ , the mean of  $\Delta T_N$  is  $4 \pm 4.7$ .

Finally, we looked into the relation between the gravitational field at  $r_{0,\text{GCS}}$  and  $M_*$ . In order to estimate it, we first need to obtain the dynamical mass enclosed by  $r_{0,\text{GCS}}$  which is approximated from the mass estimator derived by Wolf et al. (2010),

$$M_{\text{dyn}} = \frac{4\sigma_{\text{eff,gal}}^4 r_{\text{eff,gal}}}{G} \quad (8)$$

Following Harris, Harris & Alessi (2013), it is assumed as a proxy for the mass of the bulge. The velocity dispersion inside the effective radius ( $\sigma_{\text{eff,gal}}$ ) is taken from Gültekin et al. (2009) and van den Bosch (2016) and, for galaxies without information, we assume the central velocity dispersion from HyperLeda web page<sup>2</sup> (Makarov et al. 2014), based on the relation for both quantities from Gültekin et al. (2009). From this, based on the strong assumption of spherical symmetry for the mass distribution, it is possible to estimate the gravitational field at  $r_{\text{eff,gal}}$  produced by this dynamical mass,  $g_{\text{dyn,eff}}$ , which should not differ significantly from that at  $r_{0,\text{GCS}}$ . The upper panel of Fig. 6 shows the absolute value of  $g_{\text{dyn,eff}}$  versus  $M_*$ . The different symbols represent the kinematical classification of the galaxies, as indicated in the previous figures, and the colour palette represents the  $\Delta_{g-z}$  gradient up to  $r_{\text{eff,gal}}$ . The solid lines correspond to the fits obtained for the galaxies split in two mass ranges with a

<sup>2</sup><http://leda.univ-lyon1.fr>

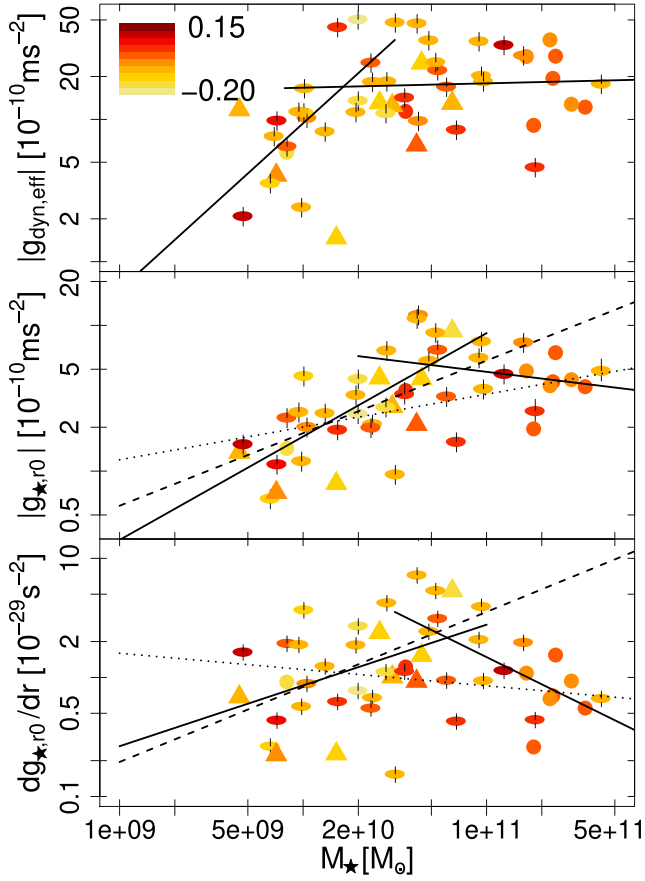


**Figure 6.** *Upper panel:* Gravitational field produced by the dynamical mass at  $r_{\text{eff,gal}}$ , as a function of the  $M_*$ . The symbol coding is the same as in previous figures. The solid lines represent the fit for galaxies in two different ranges of  $M_*$ , with the threshold at  $2 \times 10^{10} M_\odot$ . *Middle panel:* Gravitational field caused by the stellar component at  $r_{0,\text{GCS}}$ , as a function of the  $M_*$ . The symbol coding is the same as in Fig. 4. The solid lines represent the fit for galaxies in two different ranges of  $M_*$ , with the threshold at  $5 \times 10^{10} M_\odot$ . The dashed and dotted lines represent the fits for subsamples where galaxies are divided in two ranges of  $\Delta_{g-z}$ . *Lower panel:* The derivative of the gravitational field in terms of  $r$ , as a function of the  $M_*$ . The symbols and the different lines are analogues to those from the upper panel.

threshold at  $M_* = 2 \times 10^{10} M_\odot$ . From these, the resulting relation is

$$Y = -10.7 \pm 3.6 + 1.2 \pm 0.3 \times X, \quad M_* \lesssim 2 \times 10^{10} M_\odot \quad (9)$$

$$+ 0.9 \pm 0.9 + 0.03 \pm 0.09 \times X, \quad M_* \gtrsim 2 \times 10^{10} M_\odot$$

with  $X$  corresponding to  $\log_{10}(M_*)$  and  $Y$  representing the  $\log_{10}(|g_{\text{dyn,eff}}|)$ . This implies that the gravitational field at  $r_{\text{eff,gal}}$  remains constant through more than an order of magnitude in  $M_*$ .

It is also possible to calculate the gravitational field caused by the stellar component from the spatial mass distribution. Following the assumption of spherical symmetry, the luminosity enclosed at a given radius,  $r$ , the de-projection of the Sérsic profile through the expression from Lima Neto, Gerbal & Márquez (1999),

$$L_r(r) = L_{\text{tot}} \frac{\gamma \left[ (3-p)n, (r b_n^n / r_{\text{eff,gal}})^{\frac{1}{n}} \right]}{\Gamma[(3-p)n]},$$

$$L_{\text{tot}} = 2\pi n \Gamma(2n) I_{\text{eff,gal}} e^{b_n r_{\text{eff,gal}}^2} b_n^{-2n},$$

$$p \simeq 1 - \frac{1}{n} + \frac{0.05463}{n^2} \quad (10)$$

with  $\Gamma(a)$  representing the complete gamma function, and  $\gamma(a, x)$  the lower incomplete gamma function. The stellar mass enclosed at  $x$  results from the mean  $\langle ML_z \rangle$  from Bell et al. (2003) relations. Then, the assumption of spherical symmetry leads to the gravitational field at radius  $r$ ,  $g_*(r)$  and its derivative,

$$\frac{dg_*(r)}{dr} = K_{\text{GM}} \left\{ \frac{1}{n} \frac{b_n r_n^{\frac{1}{n}-1} e^{-b_n(r/r_{\text{eff,gal}})^{\frac{1}{n}}}}{r_{\text{eff,gal}}^{1/n} r^2} \left( \frac{r b_n^n}{r_{\text{eff,gal}}} \right)^{3-p-\frac{1}{n}} + \right.$$

$$\left. - \frac{2}{r^3} \gamma \left[ (3-p)n, (r b_n^n / r_{\text{eff,gal}})^{\frac{1}{n}} \right] \right\},$$

$$K_{\text{GM}} = \frac{-G \langle ML_z \rangle L_{\text{tot}}}{\Gamma[(3-p)n]} \quad (11)$$

with  $L_{\text{tot}}$  and  $p$  as presented in equation (10),  $G$  being the gravitational constant, and  $\langle ML_z \rangle$  the mean of  $\langle ML_z \rangle$  up to the radius  $x$ .

The middle panel of Fig. 6 shows the absolute value for this latter expression of the gravitational field at the core radius,  $g_{*,r_0}$ , as a function of the stellar mass of the galaxy,  $M_*$ . The symbols follow the same coding as in previous figures. The solid lines represent the linear fits for the galaxies in two ranges of  $M_*$ , with a threshold at  $5 \times 10^{10} M_\odot$ ,

$$Y = -6.9 \pm 1.4 + 0.7 \pm 0.1 \times X, \quad M_* \lesssim 5 \times 10^{10} M_\odot$$

$$+ 2.4 \pm 1.9 - 0.15 \pm 0.18 \times X, \quad M_* \gtrsim 5 \times 10^{10} M_\odot \quad (12)$$

with  $X$  corresponding to  $\log_{10}(M_*)$  and  $Y$  representing the  $\log_{10}(|g_{*,r_0}|)$ . The slopes for both fits differ, leading to a positive correlation between  $M_*$  and  $g_{*,r_0}$  for the galaxies in the low mass range, most of them FR, while the more massive ones present a slightly negative slope, in compliance with zero, suggesting a negligible correlation. If the range of colour gradient is split in halves, the linear fit for the galaxies with the lower  $\Delta_{g-z}$  values has a slope  $0.5 \pm 0.1$  (dashed line in the figure), which increases to  $0.6 \pm 0.1$  if NGC 1316, a massive merger remnant in the outskirts of the Fornax cluster, is not considered. For the galaxies with large  $\Delta_{g-z}$  values, the slope results  $0.22 \pm 0.07$  (dotted line). These latter fits span the entire mass range and suggest that the change in the relation might obey different evolutionary histories for the stellar population of the inner regions of the galaxies.

The derivative of the gravitational field at  $r_{0,\text{GCS}}$  as a function of the  $M_*$  is presented in the lower panel of Fig. 6, following the same symbol coding as in the upper panel. As it occurred for  $g_{*,r_0}$ , the linear fit differs for galaxies with  $M_* \leq 5 \times 10^{10} M_\odot$ , in comparison with their more massive counterparts,

$$Y = -5.2 \pm 2.5 + 0.5 \pm 0.2 \times X, \quad M_* \lesssim 5 \times 10^{10} M_\odot$$

$$+ 8.5 \pm 2.9 - 0.76 \pm 0.26 \times X, \quad M_* \gtrsim 5 \times 10^{10} M_\odot \quad (13)$$

with  $X$  corresponding to  $\log_{10}(M_*)$  and  $Y$  representing the logarithm of  $dg_{*,r_0}/dr$  at  $r_{0,\text{GCS}}$ . When the sample of galaxies is split in two ranges of  $\Delta_{g-z}$ , the linear fits for both subsamples differ. The one corresponding to the galaxies with lower values of  $\Delta_{g-z}$  (dashed line) presents a slope of  $0.63 \pm 0.2$  and is in agreement with that obtained for galaxies with  $M_* \leq 5 \times 10^{10} M_\odot$ , which are mainly FRs. The fit to the galaxies with larger values of  $\Delta_{g-z}$  (dotted line) is less steep and implies a negative correlation, presenting a slope of  $-0.14 \pm 0.1$ .

The overall view from the Fig. 6 indicates that the observational estimations of the gravitational field at  $r_{0,\text{GCS}}$  and its change are proportional to the stellar mass up to a few times  $10^{10} M_\odot$ . Assuming that  $r_{0,\text{GCS}}$  is a proxy of the galactocentric radius at which GCs are more susceptible to tidal disruption, it suggests that less massive galaxies require weaker gravitational fields. These behaviours are not reproduced at the massive end of the stellar mass function, populated



by central galaxies. The partition into samples according to their colour gradients reinforces these results, pointing to the relevance of the different evolutionary histories.

## 4 DISCUSSION

### 4.1 The relevance of the evolutionary pathways

Colour gradients are essential probes of the evolutionary history of galaxies since different assembly histories naturally yield contrasting gradients (e.g. Suess et al. 2019). Classic inside-out growth produces negative gradients, and once this initial dissipative phase culminates through quenching mechanisms, the galaxy continues to grow its mass by accreting bluer stars in major mergers, leading to a steeper gradient (e.g. Bezanon et al. 2009; Naab, Johansson & Ostriker 2009).

As depicted by the colour palette used across all plots in this work, the majority of the galaxies within our sample present a negative colour gradient, which is expected for local ETGs in this range of masses. However, a wide range of values is observed, and a dependence on how negative the gradient is appears when we analyse scaling relations splitting the sample into halves according to this value. This implies the assembly history of galaxies that determines the gradient also shapes the inner regions of the GCS. In the left panel of Fig. 4, galaxies with more positive gradients show a steeper correlation, indicating a larger difference in the behaviour of galaxies at the extremes of the mass range. More massive galaxies show larger values of core radius, corresponding to GCS with a flatter profile in the inner region. This is commonly attributed to mergers re-distributing GCs to the outskirts of the galaxy, which also affect the field population of massive ETGs, leading to flatter colour profiles (e.g. Tortora et al. 2010; Kennedy et al. 2016). In the lower mass end, galaxies show lower values of core radius, closer to the range covered by galaxies with more negative gradients. This might imply that the positive gradient in these galaxies might just be a consequence of shorter star formation phases (see Liao & Cooper 2023, for a discussion on the physical processes that shaped the colour gradients), with these behaviours split at approximately the pivot mass. As mentioned in Paper II, the pivot mass is associated with the point where GCSs are dominated by metal-poor GCs that come from the accretion of stripped dwarf galaxies in dry mergers, which is consistent with our scenario.

This is crucial to understand the behaviour of the relations involving  $r_{0,\text{GCS}}$  for different ranges of colour gradients. Chen & Gnedin (2022) post-processed the evolution of Milky Way-like haloes in TNG50 and tagged collisionless particles as GCs, to follow up their evolution, including estimations of mass-loss due to stellar evolution and tidal disruption. Their results suggest that median apocenter radii for *ex situ* GCs are considerably larger than those for *in situ* GCs, leading to more extended cores in the radial profiles of *ex situ* GCs. Considering that galaxies with the most negative colour gradients are FRs, it is worth considering that stellar discs might increase the disruption of GCs for galaxies with masses below  $\approx 10^{10} M_{\odot}$  (Bekki 2010). This is supported by the different relations obtained for the gravitational field caused by the stellar population at  $r_{0,\text{GCS}}$  as a function of  $M_{*}$ , when galaxies are split in halves from their colour gradient (see Fig. 6).

### 4.2 Disruption mechanisms at long term

In addition to the large-scale evolutionary processes that their host galaxy undergoes, GCs are affected by the stellar evolution of their

population, as well as dynamical processes of different types that reduce their total mass and might even entirely destroy them (e.g. Kruijssen et al. 2011). Inner processes include the expulsion of gas caused by the evolution of stars inside the GC and two-body encounters that may provide stars with enough speed to escape the cluster (Chandrasekhar 1942). Galactic tidal fields cause external dynamical processes that kinematically perturb the cluster, allowing for stars and gas to escape its gravitational influence (e.g. Gieles et al. 2006; Elmegreen & Hunter 2010; Kruijssen et al. 2011). Meiron et al. (2021) pose that all of these processes are coupled, since the time-scales are comparable, which increases the difficulty in modelling them numerically. In their work, tidal interactions rule over stellar evolution in terms of leading the mass-loss, even for weak tidal fields. Tidal field-based disruption is stronger in the inner parts of galaxies, whereas mass-loss by internal processes is ubiquitous, although it is still consistently less relevant than external processes (Rossi, Bekki & Hurley 2016; Chen & Gnedin 2022). The relevance of the external processes is also supported by observational evidence; the relative richness of GCSs in dwarf galaxies (e.g. Georgiev et al. 2010; Harris, Harris & Alessi 2013) can be interpreted in terms of a deficiency of field stars, but also as a hint of the low efficiency of disruption processes in these galaxies, particularly for those that are not embedded in intense tidal fields (Liu et al. 2019).

In the early stages of galaxy evolution, while star formation is still active in the proto-galaxy discs, these external processes are predominantly caused by tidal shocks caused by molecular clouds. When GCs approach these clouds, they heat up, thus losing stars that gain enough velocity to escape. Molecular clouds become rare in a relatively short time after star formation ends, yet GC disruption continues after the host galaxy quenches. Galaxies undergo interactions and accretion processes, which affect their GCS, as shown numerically (e.g. Brockamp et al. 2014; Bastian et al. 2020). Once tidal interactions with the interstellar medium become insufficient, GCs must be tidally shocked by other elements of the galaxy. In the case of FRs, we have already noticed that GCs can become tidally shocked after interacting with discs (see Bekki 2010). Fig. 6 shows that low-mass galaxies have small derivatives of the gravitational field at  $r_{0,\text{GCS}}$ , indicating that tidal interactions are happening even in galaxies with weak fields that do not vary much at core radius. For SRs, the lack of substructure in the stellar component would decrease the likelihood of disruption by fast tidal shocks, but the presence of a  $r_{0,\text{GCS}}$  indicates that tidal interactions are still efficient to induce mass-loss in GCs. In agreement with this, several properties of GCSs in ETGs exhibit trends with increasing galactocentric distances, i.e. with the weakening of the tidal fields experienced by GCs, such as the increase in the mean half-light radius (Jordán et al. 2005; Masters et al. 2010), as well as changes in the mass function of intermediate-age GCs in nearby merger remnants (e.g. Goudfrooij 2012).

An alternative to tidal shocks is dynamical friction, as originally proposed by Capuzzo-Dolcetta & Mastrobuono-Battisti (2009). In this mechanism, GCs are dragged through the centre of the galaxy through dynamic friction, where they get tidally disrupted. Since this is heavily dominated by the energy equipartition, more massive GCs should be mainly affected. The more massive quartiles in Fig. 3 present significantly larger values of core radius, suggesting that even if dynamical friction drags them to the inner regions of the galaxy, the tidal interactions are not efficient to disrupt them. In general, observations point to lower mass GCs being the most commonly disrupted, making dynamic friction unlikely as the dominant mechanism for massive galaxies. This might not be the case for less massive galaxies, considering that recent results from E-MOSAIC simulations found that time decays from dynamical friction

decrease towards less massive hosts (Shao et al. 2021), but numerical results suggest that cored dark matter profiles should weaken the effect of dynamical friction for dwarf galaxies, leading to decay time-scales larger than the age of the Universe (e.g. Goerdt et al. 2006; Inoue 2011; Modak, Danieli & Greene 2023).

### 4.3 Contribution of dark matter in the inner regions

Curiously, the correlations in the middle and bottom panels of Fig. 6 exhibit a changing behaviour at  $M_* \approx (2-5) \times 10^{10} M_\odot$ . This is somewhat unexpected since it implies that less massive galaxies require weaker gravitational fields from the stellar component to build up the core of the GCS. Such a trend is likely linked to the evolution of the dark matter fraction in the inner regions of ETGs, leading to a U-shape relation with the  $M_*$ , with a minimum at  $M_*$  a few times  $10^{10} M_\odot$  (e.g. Lovell et al. 2018). This behaviour is a consequence of the competition among the physical processes that ruled the star formation in galaxies. Supernova feedback is supposed to be more efficient in halting star formation in dwarf galaxies, where the potential well is shallower (Naab & Ostriker 2017; Dashyan & Dubois 2020). Therefore, massive galaxies are more efficient at converting gas into stars, producing more stars in the cores and more compact profiles that result in lower dark matter fractions for the inner regions. Conversely, in the most massive ETGs the AGN feedback process efficiently suppresses star formation, and dry galaxy mergers produce large effective radii and larger dark matter fractions (e.g. Tortora et al. 2019, and references therein). This connects with the distinct behaviour of the  $r_{0,GCS}$  against several parameters of the host galaxy for different ranges of colour gradient, depicted in previous sections.

While dark matter substructures are susceptible to disruption at long time-scales by the tidal interaction with the central halo, a fraction of them survive, as suggested by several numerical studies (e.g. Springel et al. 2008; van den Bosch & Ogiya 2018). Webb et al. (2019) studied the effect of these dark matter substructures on globular clusters. They evaluated galaxy models presenting several degrees of substructure, with subhaloes represented by both Hernquist spheres and point sources. The presence of Hernquist subhaloes does not significantly affect the star cluster evolution, but the mass-loss across the time is increased when subhaloes are treated as point sources. This is driven by close encounters with subhaloes more massive than  $10^5 M_\odot$ . Although point-source subhaloes seem like an unrealistic scenario, perturbers in the mass range  $10^7-10^8 M_\odot$  with concentrations higher than expected for field dark matter haloes of similar mass are thought to be responsible for the gaps in the Galactic stellar stream GD-1 (Bonaca et al. 2019; Banik et al. 2021). In this regard, Pavanell & Webb (2021) indicate that for Milky Way-like haloes, GCs in circular orbits at galactocentric radii of  $\approx 5$  kpc experience a decrease of the dissolution times when the fraction of substructure increases. Recently, Moliné et al. (2023) studied the subhalo population in haloes spanning nine orders of magnitude in mass. In their findings, the radial distribution for subhaloes leads to a large number of them in massive haloes. Its evolution with redshift shows no variation in their number and a progressive fall into the inner parts of the halo. Hence, the role of dark matter substructure in the disruption of GCs, and particularly in massive galaxies, cannot be ruled out.

## 5 CONCLUSIONS

In this work, we studied the inner region of the GCS for a sample of bright ETGs located in nearby clusters of galaxies, supplemented

with the results obtained from our previous studies (Papers I and II) for intermediate-luminosity ETGs. The final sample has 53 GCSs, spanning more than two orders of magnitude in  $M_*$ , and a wide range of environments, from the field to the core of clusters of galaxies. All of them were observed in  $g$  and  $z$  filters by means of *HST/ACS*, and the depth of the images in terms of the typical brightness of old GCs is similar, which enables the comparison of the results. The analysis through the three papers has been carried out in a homogeneous manner, with an emphasis on the correction of the GCS radial profile for differential completeness in order to properly quantify any variations, enhancing our measurements in the inner region. The highlights from this analysis are listed below.

(i) In the most populated GCSs, it was possible to fit the radial profiles for different quartiles of brightness. The increase of  $r_{0,GCS}$  towards fainter (i.e. less massive) GCs in these systems favours tidal shocks as the main process in the long-term erosion of GCSs. Dynamical friction could also be relevant for brighter (i.e. massive) GCs, since the change of  $r_{0,GCS}$  as a function of  $z_0$  magnitude suggests that they are dragged to inner regions, although they do not seem to be efficiently disrupted.

(ii) The  $r_{0,GCS}$  correlates with the  $M_*$  of the galaxy and its  $r_{\text{eff,gal}}$ . For this latter parameter, the relation deviates from perfect correlation, leading to values of  $r_{0,GCS}$  lower than the  $r_{\text{eff,gal}}$  for massive ETGs. Both scaling relations differ when the GCS samples are split according to the colour gradient of the host galaxy. This suggests that the merging processes and the prevalence of inside/outside stellar formation are relevant to constrain the region where GCs are disrupted.

(iii) The correlation between  $r_{0,GCS}$  and  $\sigma_0$  is less clear, and the pertinence of the central black hole of the galaxy in terms of modulating the efficiency of the processes that lead to GC disruption seems neglectable.

(iv) The richness of the GCSs in terms of the stellar mass up to  $r_{0,GCS}$ , i.e.  $T_{N,r_0}$ , remains approximately constant along the entire mass range. This implies a proportionality between the number of GCs that survive at  $z = 0$  and the  $M_*$  of the galaxy up to that radius, in contrast with the behaviour of the global richness  $T_{N,r_0}$  for ETGs, which is largely influenced by the fraction of GCs formed *ex situ* and subsequently accreted from a satellite galaxy.

(v) The proxy of the gravitational field experienced by GCs at  $r_{0,GCS}$  as a function of the  $M_*$  shows a bilinear relation independently of which mass (dynamical or stellar) is used to estimate it, with a pivot mass at  $2-5 \times 10^{10} M_\odot$ . However, the relations slightly differ depending on which of these masses is considered, and it is probably related to a variety of factors, including the fraction of dark matter inside the  $r_{\text{eff,gal}}$  as a function of  $M_*$ , the survival time of dark matter substructure, the presence of inner discs (more efficient to disrupt GCs), and how likely it is that major mergers redistributed the stellar population at inner radii, including GCs, in the past Gyr.

Large efforts have been made in recent years to shed light on the formation and early evolution of GCs, constraining numerical simulations by scaling relation at  $z = 0$ . The results presented in this study emphasize the relevance of long-term disruption processes and their necessary inclusion in the analysis of GC models.

## ACKNOWLEDGEMENTS

We thank the useful comments of the referee, which helped to improve this paper. This work was funded with grants from Consejo Nacional de Investigaciones Científicas y Técnicas de la República Argentina, Agencia Nacional de Promoción Científica y Tecnológica,

and Universidad Nacional de La Plata (Argentina). This research has made use of the NASA/IPAC Extragalactic Database (NED), which is operated by the Jet Propulsion Laboratory, California Institute of Technology, under contract with the National Aeronautics and Space Administration. This study is based on observations made with the NASA/ESA *Hubble Space Telescope*, obtained from the data archive at the Space Telescope Science Institute. STScI is operated by the Association of Universities for Research in Astronomy, Inc. under NASA contract NAS 5-26555. This research was supported in part by Perimeter Institute for Theoretical Physics. Research at Perimeter Institute is supported by the Government of Canada through the Department of Innovation, Science and Economic Development and by the Province of Ontario through the Ministry of Research and Innovation.

## DATA AVAILABILITY

All raw data from *HST*/ACS can be found in the archive.

## REFERENCES

- Banik N., Bovy J., Bertone G., Erkal D., de Boer T. J. L., 2021, *MNRAS*, 502, 2364
- Bassino L. P., Caso J. P., 2017, *MNRAS*, 466, 4259
- Bassino L. P., Richtler T., Dirsch B., 2006a, *MNRAS*, 367, 156
- Bassino L. P., Faifer F. R., Forte J. C., Dirsch B., Richtler T., Geisler D., Schubert Y., 2006b, *A&A*, 451, 789
- Bastian N., Pfeffer J., Kruijssen J. M. D., Crain R. A., Trujillo-Gomez S., Reina-Campos M., 2020, *MNRAS*, 498, 1050
- Beasley M. A., 2020, in Petr K., David J., Marek S., eds., *Reviews in Frontiers of Modern Astrophysics: From Space Debris to Cosmology*, Springer International Publishing, Berlin, p.245
- Bekki K., 2010, *MNRAS*, 401, 2753
- Bekki K., Yahagi H., 2006, *MNRAS*, 372, 1019
- Bell E. F., McIntosh D. H., Katz N., Weinberg M. D., 2003, *ApJS*, 149, 289
- Bertin E., Arnouts S., 1996, *A&AS*, 117, 393
- Bezanson R., van Dokkum P. G., Tal T., Marchesini D., Kriek M., Franx M., Coppi P., 2009, *ApJ*, 697, 1290
- Binney J., Tremaine S., 1987, *Galactic Dynamics*. Princeton Univ. Press, Princeton, NJ. Available at: <https://ui.adsabs.harvard.edu/abs/1987gady.book.....B>
- Blakeslee J. P. et al., 2009, *ApJ*, 694, 556
- Blom C., Spitler L. R., Forbes D. A., 2012, *MNRAS*, 420, 37
- Bonaca A., Hogg D. W., Price-Whelan A. M., Conroy C., 2019, *ApJ*, 880, 38
- Bronkamp M., Küpper A. H. W., Thies I., Baumgardt H., Kroupa P., 2014, *MNRAS*, 441, 150
- Calderón J. P., Bassino L. P., Cellone S. A., Richtler T., Caso J. P., Gómez M., 2015, *MNRAS*, 451, 791
- Capuzzo-Dolcetta R., Mastrobuono-Battisti A., 2009, *A&A*, 507, 183
- Caso J. P., Richtler T., Bassino L. P., Salinas R., Lane R. R., Romanowsky A., 2013, *A&A*, 555, A56
- Caso J. P., Bassino L. P., Gómez M., 2017, *MNRAS*, 470, 3227
- Caso J. P., De Bórtoli B. J., Ennis A. I., Bassino L. P., 2019, *MNRAS*, 488, 4504 (Paper I)
- Chandrasekhar S., 1942, *Principles of Stellar Dynamics*. The University of Chicago Press, Chicago, United States of America. Available at: <https://ui.adsabs.harvard.edu/abs/1942psd.book.....C>
- Chen Y., Gnedin O. Y., 2022, *MNRAS*, 514, 4736
- Cho J., Sharples R. M., Blakeslee J. P., Zepf S. E., Kundu A., Kim H.-S., Yoon S.-J., 2012, *MNRAS*, 422, 3591
- Choksi N., Gnedin O. Y., 2019, *MNRAS*, 488, 5409
- Côté P. et al., 2004, *ApJS*, 153, 223
- Dashyan G., Dubois Y., 2020, *A&A*, 638, A123
- De Bórtoli B. J., Caso J. P., Ennis A. I., Bassino L. P., 2022, *MNRAS*, 510, 5725 (Paper II)
- Della Croce A. et al., 2023, *A&A*, 674, A93
- Dirsch B., Richtler T., Geisler D., Forte J. C., Bassino L. P., Gieren W. P., 2003, *AJ*, 125, 1908
- Durrell P. R. et al., 2014, *ApJ*, 794, 103
- El-Badry K., Quataert E., Weisz D. R., Choksi N., Boylan-Kolchin M., 2019, *MNRAS*, 482, 4528
- Elmegreen B. G., Hunter D. A., 2010, *ApJ*, 712, 604
- Emsellem E. et al., 2011, *MNRAS*, 414, 888
- Fahrión K. et al., 2020, *A&A*, 637, A27
- Faifer F. R. et al., 2011, *MNRAS*, 416, 155
- Ferrarese L. et al., 2006, *ApJS*, 164, 334
- Forbes D. A., Spitler L. R., Strader J., Romanowsky A. J., Brodie J. P., Foster C., 2011, *MNRAS*, 413, 2943
- Forbes D. A., Read J. I., Gieles M., Collins M. L. M., 2018, *MNRAS*, 481, 5592
- Forte J. C., Geisler D., Ostrov P. G., Piatti A. E., Gieren W., 2001, *AJ*, 121, 1992
- Fukushima H., Yajima H., 2023, *MNRAS*, 524, 1422
- Gaspari M. et al., 2019, *ApJ*, 884, 169
- Georgiev I. Y., Puzia T. H., Goudfrooij P., Hilker M., 2010, *MNRAS*, 406, 1967
- Gieles M., Portegies Zwart S. F., Baumgardt H., Athanassoula E., Lamers H. J. G. L. M., Sipiør M., Leenaarts J., 2006, *MNRAS*, 371, 793
- Giersz M., Askar A., Wang L., Hypki A., Leveque A., Spuzem R., 2019, *MNRAS*, 487, 2412
- Girelli G., Pozzetti L., Bolzonella M., Giocoli C., Marulli F., Baldi M., 2020, *A&A*, 634, A135
- Goerd T., Moore B., Read J. I., Stadel J., Zemp M., 2006, *MNRAS*, 368, 1073
- Gómez M., Richtler T., 2004, *A&A*, 415, 499
- González-Lópezlira R. A. et al., 2022, *ApJ*, 941, 53
- Goudfrooij P., 2012, *ApJ*, 750, 140
- Gültekin K. et al., 2009, *ApJ*, 698, 198
- Harris W. E., 2009, *ApJ*, 703, 939
- Harris W. E., Kavelaars J. J., Hanes D. A., Pritchett C. J., Baum W. A., 2009, *AJ*, 137, 3314
- Harris W. E., Harris G. L. H., Alessi M., 2013, *ApJ*, 772, 82
- Harris G. L. H., Poole G. B., Harris W. E., 2014a, *MNRAS*, 438, 2117
- Harris W. E. et al., 2014b, *ApJ*, 797, 128
- Harris W. E., Harris G. L., Hudson M. J., 2015, *ApJ*, 806, 36
- Hon D. S. H., Graham A. W., Sahu N., 2023, *MNRAS*, 519, 4651
- Hudson M. J., Harris G. L., Harris W. E., 2014, *ApJ*, 787, L5
- Inoue S., 2011, *MNRAS*, 416, 1181
- Iodice E. et al., 2019, *A&A*, 627, A136
- Jordán A. et al., 2004, *ApJS*, 154, 509
- Jordán A. et al., 2005, *ApJ*, 634, 1002
- Jordán A. et al., 2007, *ApJS*, 169, 213
- Kendall M. G., 1938, *Biometrika*, 30, 81
- Kennedy R., Bamford S. P., Häußler B., Brough S., Holwerda B., Hopkins A. M., Vika M., Vulcani B., 2016, *A&A*, 593, A84
- Kim J.-h. et al., 2018, *MNRAS*, 474, 4232
- King I., 1962, *AJ*, 67, 471
- King I. R., 1966, *AJ*, 71, 64
- Ko Y., Lee M. G., Park H. S., Lim S., Sohn J., Hwang N., Park B.-G., 2019, *ApJ*, 872, 202
- Kormendy J., Bender R., 2012, *ApJS*, 198, 2
- Kravtsov A. V., Gnedin O. Y., 2005, *ApJ*, 623, 650
- Kruijssen J. M. D., 2014, *Class. Quantum Gravity*, 31, 244006
- Kruijssen J. M. D., 2015, *MNRAS*, 454, 1658
- Kruijssen J. M. D., Pelupessy F. I., Lamers H. J. G. L. M., Portegies Zwart S. F., Icke V., 2011, *MNRAS*, 414, 1339
- Kruijssen J. M. D., Pfeffer J. L., Reina-Campos M., Crain R. A., Bastian N., 2019, *MNRAS*, 486, 3180
- Lane R. R., Salinas R., Richtler T., 2015, *A&A*, 574, A93
- Larsen S. S., 1999, *A&AS*, 139, 393
- Legrand L. et al., 2019, *MNRAS*, 486, 5468
- Li H., Gnedin O. Y., 2019, *MNRAS*, 486, 4030
- Li Z.-Y., Ho L. C., Barth A. J., Peng C. Y., 2011, *ApJS*, 197, 22
- Liao L.-W., Cooper A. P., 2023, *MNRAS*, 518, 3999

- Lieberz P., Kroupa P., 2017, *MNRAS*, 465, 3775
- Lim S., Peng E. W., Côté P., Sales L. V., den Brok M., Blakeslee J. P., Guhathakurta P., 2018, *ApJ*, 862, 82
- Lima Neto G. B., Gerbal D., Márquez I., 1999, *MNRAS*, 309, 481
- Liu Y., Peng E. W., Jordán A., Blakeslee J. P., Côté P., Ferrarese L., Puzia T. H., 2019, *ApJ*, 875, 156
- Lovell M. R. et al., 2018, *MNRAS*, 481, 1950
- Ma X. et al., 2020, *MNRAS*, 493, 4315
- Madau P., Dickinson M., 2014, *ARA&A*, 52, 415
- Makarov D., Prugniel P., Terekhova N., Courtois H., Vauglin I., 2014, *A&A*, 570, A13
- Mandelker N., van Dokkum P. G., Brodie J. P., van den Bosch F. C., Ceverino D., 2018, *ApJ*, 861, 148
- Masters K. L. et al., 2010, *ApJ*, 715, 1419
- Mei S. et al., 2007, *ApJ*, 655, 144
- Meiron Y., Webb J. J., Hong J., Berczik P., Spurzem R., Carlberg R. G., 2021, *MNRAS*, 503, 3000
- Mieske S., Küpper A. H., Brockamp M., 2014, *A&A*, 565, L6
- Modak S., Danieli S., Greene J. E., 2023, *ApJ*, 950, 178
- Moliné Á. et al., 2023, *MNRAS*, 518, 157
- Naab T., Ostriker J. P., 2017, *ARA&A*, 55, 59
- Naab T., Johansson P. H., Ostriker J. P., 2009, *ApJ*, 699, L178
- Pavel N., Webb J. J., 2021, *MNRAS*, 503, 1932
- Peng E. W. et al., 2006, *ApJ*, 639, 95
- Peng E. W. et al., 2008, *ApJ*, 681, 197
- Peng E. W. et al., 2011, *ApJ*, 730, 23
- Ramos-Almendares F., Sales L. V., Abadi M. G., Doppel J. E., Muriel H., Peng E. W., 2020, *MNRAS*, 493, 5357
- Reina-Campos M., Trujillo-Gomez S., Deason A. J., Kruijssen J. M. D., Pfeffer J. L., Crain R. A., Bastian N., Hughes M. E., 2022, *MNRAS*, 513, 3925
- Rhode K. L., Zepf S. E., 2001, *AJ*, 121, 210
- Rhode K. L., Zepf S. E., 2004, *AJ*, 127, 302
- Richtler T., Bassino L. P., Dirsch B., Kumar B., 2012, *A&A*, 543, A131
- Richtler T., Husemann B., Hilker M., Puzia T. H., Bresolin F., Gómez M., 2017, *A&A*, 601, A28
- Rossi L. J., Bekki K., Hurley J. R., 2016, *MNRAS*, 462, 2861
- Salinas R., Richtler T., Bassino L. P., Romanowsky A. J., Schuberth Y., 2012, *A&A*, 538, A87
- Schlafly E. F., Finkbeiner D. P., 2011, *ApJ*, 737, 103
- Schuberth Y., Richtler T., Hilker M., Dirsch B., Bassino L. P., Romanowsky A. J., Infante L., 2010, *A&A*, 513, A52
- Scott N., Davies R. L., Houghton R. C. W., Cappellari M., Graham A. W., Pimblet K. A., 2014, *MNRAS*, 441, 274
- Sereno M., 2016, *MNRAS*, 455, 2149
- Sersic J. L., 1968, Atlas de Galaxias Australes, Observatorio Astronómico de Córdoba, Córdoba, Argentina. Available at: <https://ui.adsabs.harvard.edu/abs/1968adga.book.....S>
- Sesto L. A., Faifer F. R., Smith Castelli A. V., Forte J. C., Escudero C. G., 2018, *MNRAS*, 479, 478
- Shao S., Cautun M., Frenk C. S., Reina-Campos M., Deason A. J., Crain R. A., Kruijssen J. M. D., Pfeffer J., 2021, *MNRAS*, 507, 2339
- Sirianni M. et al., 2005, *PASP*, 117, 1049
- Springel V. et al., 2008, *MNRAS*, 391, 1685
- Strader J., Brodie J. P., Forbes D. A., 2004, *AJ*, 127, 295
- Suess K. A., Kriek M., Price S. H., Barro G., 2019, *ApJ*, 877, 103
- Torniamanti S., Pasquato M., Di Cintio P., Ballone A., Iorio G., Artale M. C., Mapelli M., 2022, *MNRAS*, 510, 2097
- Tortora C., Napolitano N. R., Cardone V. F., Capaccioli M., Jetzer P., Molinaro R., 2010, *MNRAS*, 407, 144
- Tortora C., Posti L., Koopmans L. V. E., Napolitano N. R., 2019, *MNRAS*, 489, 5483
- Tully R. B. et al., 2013, *AJ*, 146, 86
- Usher C., Brodie J. P., Forbes D. A., Romanowsky A. J., Strader J., Pfeffer J., Bastian N., 2019, *MNRAS*, 490, 491
- van den Bosch R. C. E., 2016, *ApJ*, 831, 134
- van den Bosch F. C., Ogiya G., 2018, *MNRAS*, 475, 4066
- Vanzella E. et al., 2022, *ApJ*, 940, L53
- Villegas D. et al., 2010, *ApJ*, 717, 603
- Webb J. J., Bovy J., Carlberg R. G., Gieles M., 2019, *MNRAS*, 488, 5748
- Wolf J., Martinez G. D., Bullock J. S., Kaplinghat M., Geha M., Muñoz R., Simon J. D., Avedo F. F., 2010, *MNRAS*, 406, 1220
- Zepf S. E., Ashman K. M., 1993, *MNRAS*, 264, 611

## APPENDIX A

**Table A1.** Galaxies analysed in Papers I and II, listed in decreasing *B*-band luminosity. The core radius, expressed in kiloparsecs, was calculated from the parameter fitted to the radial profile and the distance assume for each galaxy, both indicated in table 4 of Paper I and table 2 of Paper II. Its uncertainty comes from that fitted to the data, and the typical error in the distances, assumed as 5 per cent.

Name	$r_{0,GCS}$ (kpc)
NGC 1404	$3.2 \pm 0.4$
NGC 4526	$3.5 \pm 0.4$
NGC 1380	$3.4 \pm 0.3$
NGC 4552	$2.4 \pm 0.4$
NGC 3818	$1.5 \pm 0.2$
NGC 1340	$3.8 \pm 0.6$
NGC 4621	$1.3 \pm 0.3$
NGC 4473	$1.9 \pm 0.3$
NGC 1387	$4.7 \pm 0.6$
NGC 1439	$2.2 \pm 0.3$
NGC 4459	$2.8 \pm 0.4$
NGC 4442	$1.9 \pm 0.3$
NGC 1426	$2.4 \pm 0.4$
NGC 7173	$2.3 \pm 0.6$
NGC 4435	$1.5 \pm 0.2$
NGC 4371	$0.7 \pm 0.2$
IC 2006	$2.2 \pm 0.3$
NGC 4570	$1.3 \pm 0.2$
NGC 4267	$5.2 \pm 1.1$
NGC 4033	$1.6 \pm 0.2$
NGC 4417	$2.8 \pm 0.4$
NGC 1351	$1.6 \pm 0.1$
NGC 4564	$1.3 \pm 0.2$
NGC 1339	$2.6 \pm 0.3$
NGC 1172	$3.1 \pm 0.4$
NGC 3377	$1.4 \pm 0.2$
NGC 4434	$1.0 \pm 0.1$
NGC 4660	$2.4 \pm 0.3$
NGC 4474	$1.7 \pm 0.2$
NGC 4377	$2.2 \pm 0.3$
NGC 1419	$2.6 \pm 0.3$
NGC 1336	$2.2 \pm 0.2$
NGC 4387	$1.9 \pm 0.3$
NGC 1380A	$2.0 \pm 0.3$
NGC 4458	$1.5 \pm 0.2$
NGC 4483	$1.2 \pm 0.2$
NGC 4623	$1.1 \pm 0.1$
NGC 4352	$2.6 \pm 0.4$
NGC 4515	$1.6 \pm 0.2$
NGC 1380B	$1.9 \pm 0.2$
NGC 1428	$2.0 \pm 0.3$
FCC 255	$0.9 \pm 0.2$

This paper has been typeset from a  $\text{\LaTeX}$  file prepared by the author.